Revealing Hydroxyapatite Nanoparticle Surface Structure by CO Adsorption: A Combined B3LYP and Infrared Study

UNIVERSITÀ DEGLI STUDI DI TORINO

Revealing Hydroxyapatite Nanoparticles Surface Structure by CO Adsorption: a Combined B3LYP and Infrared Study

*Fabio Chiatti, Marta Corno, Yuriy Sakhno, Gianmario Martra and Piero Ugliengo**

Dipartimento di Chimica, University of Torino and NIS – Nanostructured Interfaces and Surfaces, Via P. Giuria 7, 10125, Torino, Italy

*Corresponding author. Phone: +39-011-6704596, E-mail: piero.ugliengo@unito.it

Abstract

The adsorption of CO at hydroxyapatite (HA) surfaces has been studied by combining quantum mechanical modeling with experimental IR results. To model the adsorption, the hybrid B3LYP-D*, inclusive of dispersive interactions, has been adopted within the periodic boundary conditions, using the CRYSTAL09 program and a polarized Gaussian type basis set. Four HA surfaces have been investigated using slabs of finite thickness: two stoichiometric HA(001) and HA(010)R surfaces and two non-stoichiometric HA(010) in which the value of the Ca/P ratio was either higher (HA(010)_Ca-rich) or lower (HA(010)_P-rich) than the bulk value. Geometrical, energetic and vibrational features of the adsorption process have been fully investigated, by considering CO coverage ranging from 1.5 to 6 CO/nm^2, respectively. By combining the results from the modeling study with experimental IR data, it was assessed that the vibrational features of adsorbed CO can be proposed as a potential tool for the recognition of types of surface terminations exposed by HA crystalline nanoparticles.

Keywords: hybrid functionals, carbon monoxide, biomaterial surfaces, vibrational spectra

Introduction

In the last 50 years, the complex and multidisciplinary field, related to the properties of biomaterials, has raised considerably.[1] The biomaterial class envisages all those organic and inorganic compounds which elicit and promote an appropriate function or response when interacting with biological systems. Among these compounds, hydroxyapatite [HA, $Ca_{10}(PO_4)_6(OH)_2$] has been the subject of many studies, because of its intrinsic biocompatibility as main constituent of the natural biological bone and teeth tissues.[2-4]

Indeed, not only natural-derived, but also synthetic HA materials are directly employed for building prostheses, for coating metallic implants and in repairing/replacing damaged enamels (pathological calcifications diseases, as tumors or osteoporosis).[4-7] In these applications, HA is able to stimulate the osteo-integration, enhancing the fixation of the prostheses by avoiding the undesired immune response of rejection.

Interestingly, HA is not limited to applications in a biomedical context, as it has become a promising material in heterogeneous catalysis as well. For instance, HA powders are often employed in the green-chemistry field, as a support for metal nanoparticles deposition. Jaworski et al.[8] have recently studied the reactivity of the HA surfaces to support cobalt nanoparticles. This hybrid system showed very interesting catalytic properties for the production of hydrogen molecules from the hydrolysis of sodium borohydride ($NaBH_4$). Zahmaktran et al.[9] showed that rhodium clusters supported by HA successfully catalyze the hydrogenation of aromatic compounds in solvent-free conditions.

Remarkably, also HA as such can successfully elicits catalytic behaviors. By modulating the Ca/P ratio, HA can promote the dehydroxylation reaction of alcohols, such as ethanol or 1-butanol, or, conversely, the hydroxylation of unsaturated systems, such as the synthesis of phenol from benzene.[10-12]

Despite such a variety of applications, most of the which have not been listed here for the sake of brevity, few studies have focused, at the molecular level, on the HA surface structures,

which are directly involved in the adsorption processes and govern the chemical activity of HA, either when contacting biological molecules or as a catalyst. One example focusing on an atomistic view is the work by the Kandori's group,[13] who reported that only two families of different binding sites, called C and P sites, respectively, are present on well-defined hexagonal HA crystal planes. The C sites, arranged in a rectangular arrays on *ac* (or *bc*) faces and rich in Ca^{2+} ions, act as adsorbing sites for acidic proteins, whereas the P sites, arranged hexagonally on *ab* faces and lacking Ca^{2+} ions, are more inclined to adsorb basic proteins.[14] Moreover, some of us[15-16] have analyzed the morphologies and surface structures of nano-sized HA particles, from different syntheses, using high-resolution transmission electron microscopy (HR-TEM) and infrared (IR) spectroscopy, in controlled atmosphere and thermal treatment conditions of the samples. It was shown that, in these cases, the crystalline order was extended up to the particles surfaces, whose dominant crystal forms were, in general, of the {010} type. Sato et al.[17] demonstrated also by HR-TEM that the (010) surface exhibits three different terminations, as also recently remarked by Ospina et al.,[18] even if they did not analyze the detailed features of the terminations. Nevertheless, a precise HR-TEM recognition of subtle differences in the surface structure of HA nanoparticles is a really difficult task and requires advanced instruments and data analysis skills. On the contrary, the study of adsorbed probe molecules, exhibiting features which are sensitive to the adsorbing sites structure, offers the possibility to obtain information at a molecular resolution with less effort. Along that line, some of us[19-20] have characterized the HA nano-crystals morphology by a joint use of infrared spectroscopy, HR-TEM techniques and quantum mechanical calculations to monitor the vibrational bands of the adsorbed glycine as a probe of the specific features of exposed surfaces. The results were unequivocally indicating that the (010) family of crystal planes is dominating the nano-crystals morphology.

While glycine is a complex probe, as it can interact simultaneously with C and P kinds of sites, carbon monoxide (CO) has been adopted since long ago due to its simplicity. When adsorbed on surfaces, it allows for a fine characterization of the Lewis surface acidity, by

monitoring the response of its stretching mode due to adsorption.[21] Recently, some of us[15] have reported IR measurements of CO adsorption at 100K on dehydrated crystalline HA surfaces, indicating some heterogeneity of Lewis acid sites, also confirmed by other studies based on adsorption microcalorimetry measurements and quantum mechanical modeling.[22] Nonetheless, the attempt to classify the relative importance of each HA surface in the HA nano-crystals morphology was partly unsatisfactory. Starting from those preliminary results, in this paper we have studied in much more details the CO adsorption at the HA surfaces, by means of quantum mechanical modeling and IR technique. As already done in previous papers dealing with glycine as a probe,[19-20] we have modeled the adsorption of CO, from low to high CO coverages, on periodic models of the most relevant HA surfaces, within periodic boundary conditions. The quantum mechanical problem was solved using polarized triple-ζ all-electron Gaussian basis set, more extended than those adopted in the past, and the hybrid B3LYP-D* functional, which guarantees good accuracy in structures, energetic (as it includes dispersion interactions) and vibrational features. We have considered four slab models which should reproduce the most important terminations of HA: the stoichiometric HA(001) and HA(010) surfaces and the non-stoichiometric HA(010)_Ca-rich and HA(010)_P-rich surfaces. The stoichiometric HA(010) surface has been considered in its water-reacted form, being water ubiquitous in all body fluids and HA synthesized in a watery environment (the stoichiometric HA(010) is the only surface upon which water dissociates). The theoretical modeling of the two non-stoichiometric (010) surfaces has already been performed by Astala and Stott with the PBE functional and the SIESTA program.[23] As already mentioned, in a previous paper,[22] the adsorption of CO was limited to very low coverage (one CO molecule *per* each HA surface), which did not allow for a complete understanding of the experimental data. In the present paper, we have increased the loading from 1 up to 4 molecules *per* unit cell of each considered surface model. We anticipate that the joint use of IR experimental data and quantum mechanical modeling allowed to reveal the relative importance of the HA crystal surfaces in dictating the morphology of the HA nano-

crystals.

Materials

Hydroxyapatite nanocrystals were prepared by dropping a solution of H_3PO_4 (1.26 M, 0.6 L) into a $Ca(OH)_2$ suspension (1.35 M, 1.0 L), to accomplish the reaction:

$$10\ Ca(OH)_2 + 3\ H_3PO_4 \rightarrow Ca_{10}(PO_4)_6OH_2 + 9\ H_2O$$

The reaction mixture was stirred under N_2 atmosphere for 24 hours at 368 K. The stirring was then suspended and the mixtures were left standing for 2 hours to allow for deposition of the inorganic phase. The HA powders were then isolated by filtration of the mother liquor, repeatedly washed with water and dried at room temperature. The material exhibited a specific surface area of ca. 70 m^2/g, (N_2 adsorption at T ≈77K, BET method, ASAP 2020 Micromeritics) and a Ca/P ratio of 1.65 (the stoichiometric one being 1.67). Carbon monoxide used for IR measurements was of the high purity type (Praxair), and dosed onto the sample without any further purification except liquid nitrogen trapping.

Experimental methods

To prepare for IR study of adsorbed CO, HA powder was pressed in a self-supporting pellet ("optical thickness" in the 15-20 mg/cm^2 range) and placed in an home-made IR cell for the collection of spectra at ca. 100 K,[24] equipped with KBr. The cell was connected to a conventional vacuum line (residual pressure: 1×10^{-5} mbar, 1 mbar=102 Pa), allowing all thermal treatments and adsorption–desorption experiments to be carried out *in situ*. Before IR measurements, the sample was outgassed at 433 K, which ensured the best compromise between a high extent of water removal from surface Ca^{2+} ions (ca. 85%) and limited surface modification

(in terms of loss of capability to reabsorb water).[15] Measurements were carried out at a resolution of 4 cm^{-1} using a Vector 22 spectrometer, equipped with a MCT detector. Spectra of adsorbed CO are reported in Absorbance, after subtraction of the spectra of the samples before CO admission as the background.

Computational details

The interaction between HA surfaces with CO molecules was simulated using the CRYSTAL09 periodic code.[25-26] Graphical manipulations have been carried out with the molecular graphics program MOLDRAW [27] and QUTEMOL.[28]

Basis set

The multi-electron wave function was described by a linear combination of crystalline orbitals expanded in terms of Gaussian-type basis set functions. In the present work, Ca atoms were described with a triple-ζ valence all-electron basis set, 86-811G(3d), with α_{sp} = 0.295 $bohr^{-2}$ as the exponent of the most diffuse shell and α_{pol} = 0.3191 $bohr^{-2}$ for polarization.[29] A 85-21G(d) basis set was used for P atoms, with α_{sp} = 0.1350 $bohr^{-2}$ as the most diffuse shell exponent and α_{pol} = 0.7458 $bohr^{-2}$ for polarization. C atoms were represented with a 511111-411G(d) basis set (VTZ), with α_{sp} = 0.1008 $bohr^{-2}$ as the most diffuse shell exponent and α_{pol} = 0.8000 $bohr^{-2}$ for polarization.[30] O atoms were represented with a 511111-411G(d) basis set (VTZ), with α_{sp} = 0.1751 $bohr^{-2}$ as the most diffuse shell exponent and α_{pol} = 0.1200 $bohr^{-2}$ for polarization.[30] H atom was described with a 31G(p) basis set, with α_{sp} = 0.1613 $bohr^{-2}$ as the most diffuse shell exponent and α_{pol} = 1.100 $bohr^{-2}$ for polarization. This basis set has been successfully adopted to study the adsorption of glycine on the HA surfaces.[20]

Hamiltonian and geometry optimization

All calculations were performed within the Density Functional Theory (DFT) framework with the B3LYP hybrid functional. This functional has already proved to provide results in good

agreement with the experimental data for similar systems.[31-33] The Hamiltonian matrix was diagonalized on 4 *k*-points. Default values (6 6 6 6 14) of the tolerances controlling the accuracy of the Coulomb and exchange series were adopted. The SCF was considered converged with a difference between the energies lower than 10^{-7} Hartree. Atomic coordinates optimization was performed *via* an analytical gradient method, upgrading the numerical Hessian with the Broyden-Fletcher-Goldfarb-Shanno algorithm.[26]

Adsorption energies

The scheme to compute the adsorption energies is the one described by some us for similar systems.[20, 32, 34] In essence, the electronic interaction energy *per* adsorbed CO molecule is computed using the following formula:

$$\Delta E = \left[\mathrm{E(HA\_s/}n\,\mathrm{CO)} - \mathrm{E(HA\_s)} - n\,\mathrm{E(CO)}\right]/n$$

In which E(HA_s/*n* CO), E(HA_s) and E(CO) are the total electronic energies of: i) the HA surface with *n* adsorbed CO molecules in the unit cell; ii) the bare HA_s surface unit cell; iii) the free CO molecule. On the fully optimized B3LYP geometries, a single point evaluation of the contribution due to dispersion interactions has been computed by means of the revised parameterization[35] (known as B3LYP-D*) of the original Grimme's one[36] available in CRYSTAL09. This contribution, as well as the correction of the electronic interaction energies due to basis set superposition error, have been worked out using the same formula as above. Negative ΔE values show favorable adsorption. As the dispersion is evaluated on B3LYP optimized structures, its role is expected to be somewhat underestimated compared to a full B3LYP-D* optimization as the B3LYP-D* intermolecular distances would be shorter (increasing the dispersive contribution) than the corresponding B3LYP ones. This effect may be artificially enhanced by the relatively large BSSE associated with the present basis set, so that we prefer to avoid full B3LYP-D* optimization.

Phonon frequencies and comparison with experimental IR spectra

The B3LYP vibrational frequencies, restricted to the CO fragment only, were computed

at the Γ point within the harmonic approximation, by obtaining the eigenvalues from the diagonalization of the mass-weighted Hessian matrix.[37] This strategy has been validated by some of us in the past[38] and already adopted in some previous works.[39]. The coordinates of each atom of the CO molecule were displaced by ±0.003 Å in order to compute the Hessian matrix, resulting in 5 low frequency modes associated to frustrated translation and hindered rotation and one high frequency mode associated to the CO stretching mode. The infrared intensity of each normal mode were computed using the Berry phase approach.[40] The set of frequencies has also been used to correct the purely electronic interaction energies for the zero point energy and to arrive to the final enthalpy of adsorption ΔH at room temperature.

To correct for systematic errors of the B3LYP method and for anharmonicity, the B3LYP CO stretching frequency was rescaled using the scaling factor s_{resc} computed as the ratio between the experimental CO stretching frequency value and the corresponding B3LYP one:

$$s_{resc} = \frac{\nu_{\mathrm{exp}}(\text{free CO})}{\nu_{\mathrm{B3LYP}}(\text{free CO})} \tag{1}$$

For each optimized structure i, the IR spectrum $S_i(\nu)$ in the CO stretching region was computed as a linear combination of Gaussian functions $G(\nu - \nu_j)$, each one centered at the j^{th} CO B3LYP rescaled frequency value ν_j, and a 15 cm^{-1} full width at half maximum (FWHM), weighted by the corresponding IR intensity (I_j):

$$S_i(\nu) = \sum_j I_j \cdot G(\nu - \nu_j) \tag{2}$$

A linear combination $T(\nu)$ of all the computed $S_i(\nu)$ spectra represents the resulting spectrum in which, however, the weights w_i of each $S_i(\nu)$ have to be, somehow, determined:

$$T(\nu) = \sum_i w_i \cdot S_i(\nu) \tag{3}$$

The criterion adopted to choose the weights w_i has been to run a non-linear regression

between the experimental IR spectrum and the computed $T(\nu)$ one, by keeping constant the relative ratios of the computed I_j intensities within the same case *i*, while changing their absolute values.

Results and discussion

Slab models

The quality of the present basis set is better than the one adopted recently to model bulk HA structure and vibrational features. The comparison between computed and experimental features for the bulk have been proved to be very good and the interested reader can found details in Ref. [41-42] Previous studies, both theoretical[43] and experimental,[19] have revealed that the most important surfaces of hydroxyapatite are the HA(001) and the HA(010) ones. Indeed, from the experimental side, crystalline HA nanoparticles with platelet morphology, exposing (010) planes as basal surfaces (with sides in the 40–100 nm range), and (001) and (100) planes (the latter being isostructural with the (010) one) as lateral terminations (resulting in a particles thickness of ca. 5 – 10 nm), have been used.[15]

The HA(001) surface model has already been described in related papers by some of us (see Ref.[43] and references therein). This surface, in which the OH^- ions are aligned perpendicularly to the slab plane, exhibits a dipolar moment across the slab which should, in principle, affect the stability with the increasing of the thickness. Nonetheless, we recently proved that the growth of the dipole moment magnitude with the slab thickness is non-critical in terms of stability of the electronic structure, at least up to a nanometric scale.[44] Therefore we have adopted a dipolar HA(001) model for all simulations, with a thickness of 13.5 Å. A top view of all considered surface is displayed in Figure 1 (top-left panel).

The {010} crystal plane family is composed of a sequence of layers like …A-B-A-A-B-A-A-B-A-…., where the A and B layers have the $Ca_3(PO_4)_2$ and $Ca_4(PO_4)_2(OH)_2$ chemical compositions, respectively. Hence, for a well-defined (010) slab, the most exposed layers result as ...-A-B-A, ...-A-A-B or ...-B-A-A giving rise to the stoichiometric HA(010) and the non-stoichiometric HA(010)_Ca-rich and HA(010)_P-rich surfaces, respectively (Figure 1, bottom-left and right panel, respectively). The thickness values of the adopted models for these surfaces are 17.2 Å, 19.2 Å and 20.0 Å, respectively. We found that the HA(010) stoichiometric surface

reacts spontaneously with water, generating new superficial POH and CaOH functionalities. As HA is experimentally synthesized in a watery environment, we considered the water-reacted form, HA(010)R (Figure 1, top-right panel), to be more representative of the stoichiometric termination than the pristine unreacted HA(010) for modeling a real surface.[20, 23, 43] As all the three terminations have been shown to be important,[20, 22] we considered all of them for CO adsorption.

These four surfaces have been relaxed, keeping the cell parameters fixed at the HA bulk values, while allowing the atomic positions to move without symmetry constraints. Through the analysis of the resulting electric field, we studied the electrostatic behavior of each site of the surfaces. Then, following the electronic complementarity principle between electrostatic potential values of adsorbent/adsorbate, already adopted in other similar studied,[43, 45] the CO molecules have been adsorbed C-down at the surface Ca^{2+} ions. The adsorption in a O-down fashion has been long established not to be relevant for CO adsorbed on surfaces of ionic and semi-ionic oxides.[21] We have started adsorbing one CO molecule *per* surface unit cell, allowing the atomic internal coordinates to relax. This procedure has been repeated until four CO molecules per unit cell were adsorbed, which covered all the exposed Ca^{2+} ions. During this step, we observed that the initial adsorption CO position was, most of the times, changed during the geometry optimization as CO were seeking the most active Ca^{2+} site available for adsorption for each particular CO loading.

Energetic analysis

Following the procedure described in the Computational Details section, the energetic values for each model structure, reported in Table 1, have been computed (more details in the Electronic Supplementary Information, hereafter ESI). Some trends common to all cases can be underlined.

Firstly, the electronic adsorption energy ($-\Delta E^C$) exhibits an almost monotonous decreasing trend with respect to the CO loading, in agreement with what generally found in

similar calculations.[43] This is basically due to the balance between maximizing the electrostatic attractive interaction with the exposed surface Ca^{2+} ions and reducing the CO/CO lateral repulsion (both of electrostatic and exchange repulsion nature).

The dispersive contribution to the adsorption energy has been shown to be important also for the adsorption on surfaces of ionic and semi-ionic oxides, as it is the present case.[46-48] As expected, the dispersive contribution to the enthalpy ($-\Delta E^D$) increases with the CO loading, as each adsorbed molecule laterally interacts with an increasing number of adsorbed CO molecules.

Independently on the considered model, the zero-point and thermal corrections reduce the adsorption energy (it becomes less negative) by ≈3.5 kJ/mol. In all cases, the enthalpy calculated at room temperature, $\Delta H(RT)$, is highest for the adsorption of the first CO molecule (the highest among all cases is for the 1CO/HA(010)_P-rich model, about -35 $kJ \cdot mol^{-1}$). At increasing CO loading, $\Delta H(RT)$ becomes less negative reaching a plateau of about -20 kJ/mol for all cases. This trend is at variance with the decrease of the electronic adsorption energy $-\Delta E^C$: the decrease is, however, compensated by the attractive dispersive contribution which increases with the CO loading. This trend is in qualitative agreement with previous experimental microcalorimetric results, which have highlighted two classes of adsorption sites.[22] The first class of sites is important at very low CO loadings and envisages differential heat of adsorption of about -40 kJ/mol. The second class is relevant for higher CO loading, with the differential heat of adsorption value decreasing down to -10 kJ/mol.

Among electrostatic and dispersion interactions, also charge transfer within the surface/adsorbate system can contribute to the final adsorption energy. The Born dynamic charges, computed during the evaluation of the infrared intensity, have been used to study this effect. For all considered systems, the electronic charge transfer resulted very small (about 0.03 e), and almost constant for all systems (details available in the ESI). Considering that, by neglecting the BSSE, the charge transfer will be overestimated, it can be concluded that the interaction between CO and HA model surfaces is mainly due to electrostatic and dispersive

interactions.

It is worth to notice that for HA(010)R, HA(010)_Ca-rich and HA(010)_P-rich surfaces the adsorption is characterized by more than one CO per Ca ion (see Figure S1 in the ESI). The formation of poly-adducts (basically of a di-carbonyl type) mainly driven by electrostatic interaction with the adsorbing sites, have been reported for CO adsorbed in in zeolites exchanged with both alkaline[49] and alkali-earth cations as charge-balancing species.[50] On truly external surfaces, the co-adsoprtion of two CO molecules on d° cationic sites has been observed on highly coordinatively unsaturated Mg^{2+} exposed at the corners of MgO cubelets.[51] To the best of our knowledge, such ad-species have not been reported/proposed yet for adsorbing sites exposed by low index surfaces, as in the present case. This is no surprise, as for the surfaces of common oxides and halides (MgO, NaCl and alike) the cationic sites (Mg^{2+}, Na^{+}) are tightly packed by *atomic* anions (O^{2-}, Cl^{-}), resulting in an efficient charge screening preventing the adsorption of more than one CO per cationic site. For the present case, the anionic species are phosphate groups which less efficiently screen-out the Ca^{2+} ions due to a looser packing and a reduced charge/density ratio compared to small atomic anions. The final affinity for CO of the Ca ions exposed at the HA surfaces is then a subtle balance of the screening electrostatic effects and the exchange repulsions dictating the steric repulsion.

Vibrational analysis and comparison with experimental IR spectrum

On the optimized CO/HA structures, the IR vibrational frequencies at Γ-point, limited to the adsorbed CO molecules, have been computed at the B3LYP level, with the purpose to carry out a detailed comparison with the experimental results (*vide infra*), All the vibrational data are listed in Table 2: from the analysis of each specific HA/CO interaction, two classes of surface interacting sites can be recognized, in agreement with the energetic data reported above. The first class includes the most acidic Ca^{2+} sites, with $Ca^{2+\cdots}CO$ distance in the 2.7/2.8 Å range and a bathochromic shift of the CO stretching frequency ≥ +30 cm^{-1}. The second class envisages weaker sites, the $Ca^{2+\cdots}CO$ distance being longer (2.9/3.0 Å) and the bathochromic CO shifts

smaller (+15 cm^{-1}). A different kind of low-acidic site, present in the HA(010)R models, has been revealed by 2 CO loading per unit cell case, in which also the OH^- ion is involved in an $OH^{\cdots}CO$ interaction. This site belongs to the class of weaker acidity, as the corresponding bathochromic CO shifts are around +15 cm^{-1}.

One objective of the present work is to use the IR spectroscopy of the adsorbed CO for detecting the surface terminations of HA nanoparticles. To that purpose, ν(CO) spectra were simulated on the basis of the B3LYP vibrational features: the spectral profiles obtained for increasing amount of adsorbed CO on each HA surface are shown in Figure 2. The four considered HA surfaces appeared almost undistinguishable, if only one CO molecule per surface unit cell was considered (top-left panel). Only by the co-adsorption of more than one CO molecule per Ca^{2+} site (i.e. at higher CO loading) the ν(CO) spectral profiles start to increase in complexity. When CO is co-adsorbed on the same Ca^{2+} site, each CO molecule probes the field of a farther zone around the Ca^{2+} site compared to the case of one CO per Ca ion. This subtle effect, which increases the complexity of the IR spectrum, has been characterized more clearly for CO adsorbed on Ni^{2+} ions embedded in an amorphous silica matrix.[52-53]

The B3LYP ν(CO) spectra have been used to analyze the experimental IR spectra of CO adsorbed at ca. 100 K on HA nanoparticles, obtained by progressively decreasing the CO pressure from an initial value of 25 mbar (Figure 3). Higher CO pressure essentially resulted only in an increase in intensity of the component at 2140 cm^{-1} due to CO adsorbed in a liquid-like form, indicating that all cationic surface sites available for a specific interaction with probe molecules were already occupied. The spectrum taken at the highest CO coverage (curve a) exhibited a main band with maximum at 2168 cm^{-1}, a full width at half maximum of ca. 20 cm^{-1} and a weak shoulder at ca. 2145 cm^{-1}. This latter component resulted from the superimposition of the roto-vibrational profile of CO gas in equilibrium with the sample (significantly contributing to the spectra $p_{CO} \geq 4$ mbar, curve b) and a partly resolved component due to adsorbed species

(more clearly appearing for $p_{CO} \leq$ 2 mbar, see curve c in the inset with the zoomed view of the spectral range indicated as "A"). By decreasing the CO coverage, the band intensity progressively decreased and the maximum shifted to higher frequency (curves b-j). The evolution of the main component at 2168 cm^{-1} appeared mirrored by the progressive vanishing of a very weak component in the 2135-2105 cm^{-1} range (Figure 3, inset). The ratio between the positions of these two signals (e.g.: 2122/2171 and 2131/2179 = 0.978) corresponds to the $(\mu(^{12}CO)/\mu(^{13}CO))^{1/2}$ ratio, where μ is the CO reduced mass. By considering the relative intensity of the two components, the weakest one can be attributed to ^{13}CO molecules present in natural abundance (ca. 1%). In a previous paper by some of us,[15] the progressive up-shift of the signal at 2168 cm^{-1} with the decreasing of the CO coverage, has been attributed to the decrease of CO-CO interactions, both static and dynamic in nature. This is known to occur between arrays of CO molecules adsorbed on other insulating materials, like NaCl,[54] MgO[55] and Al_2O_3.[24] At that time, not enough care was devoted to check the presence of the $\nu(^{13}CO)$ weak signal, now observed at 2122 cm^{-1} (after the disappearance of the contribution due to CO gas, Figure 3, curve d): the position of this signal is highly informative on the absence of any dipolar (dynamic) coupling, which would require the presence of *parallel* ^{13}CO vibrating dipoles, among ^{12}CO adsorbed molecules. In brief, when $^{12}CO/^{13}CO$ mixtures poor in ^{13}CO ($\leq$ 10%) are used, both molecules experience adsorbate-adsorbate static interactions (mainly through the HA solid), which induce a *decrease* of the ν(CO) frequency with respect to the singleton ($\theta_{CO} \rightarrow 0$). Conversely, dynamic coupling, which induces an *increase* of the ν(CO) frequency with respect to the singleton, only occurs among arrays of CO adsorbed in a parallel fashion and vibrating with similar frequency. This is the case of large patches of ^{12}CO molecules, whereas is not effective for the few ^{13}CO adsorbed molecules highly dispersed in the ^{12}CO patches. Thus, when ^{12}CO and ^{13}CO are adsorbed in the form of arrays of parallel mono-carbonylic adducts, a difference, corresponding to the extent of the dynamic coupling, should occur between the

position of the observed $\nu(^{13}CO)$ signal (not affected by the dynamic coupling) and the position calculated as $(\mu(^{12}CO)/\ \mu(^{13}CO))^{1/2} \times \nu(^{12}CO)$ for an array of ^{13}CO molecules, (affected by the dynamic coupling).[56] Moreover, as the effectiveness of the dynamic coupling also depends on the distance among vibrating CO dipoles, it must be considered that distances among Ca^{2+} ions exposed by the calculated surfaces (Table 4S of ESI) are similar to those among Al^{3+} sites on (110) facets of δ-Al_2O_3 nanoparticles, where adsorbed CO molecules were found to experience a significant dynamic coupling.[24] Hence, it can be concluded that the coincidence between the present observed $\nu(^{13}CO)$ signal at 2122 cm^{-1} and the value resulting from the $(\mu(^{12}CO)/\ \mu(^{13}CO))^{1/2} \times \nu(^{12}CO)$ formula indicates the absence of dynamic coupling between CO molecules adsorbed on the considered HA nanoparticles, in agreement with the possible occurrence of co-adsorption of more than one CO molecule per Ca^{2+} ion, on which CO oscillators are not parallel to each other.

Focusing now on the highest CO coverage attained, it is self-evident that none of the B3LYP ν(CO) profiles (Figure 2) fits the experimental one (Figure 3, curve a). Thus, by adopting an approach similar to the adsorption of glycine on HA,[19] a weighted linear combination of the B3LYP spectra for all separated cases was carried out, seeking for the best match with the experimental IR spectrum (see Computational section for details). This procedure revealed the relative importance of the considered cases in an unbiased way, as the procedure was started by setting to unity *all* the weights w_i. After the refinements, only two models exhibited w_i values significantly different from zero, among all the considered models. These two cases are the 4CO/HA(010)_Ca-rich and the 2CO/HA(010)_P-rich (Figure 4), with the w(4CO/HA(010)_Ca-rich)/w(2CO/HA(010)_P-rich)=1/3. Figure 5 reports the two resulting B3LYP spectra, whose sum is in striking correspondence with the experimental spectrum. The evolution of the spectral pattern by decreasing the CO coverage should then results from the combination between the components resulting from the conversion of CO poly-adducts in progressively simpler adsorbed

species.

This result is in good agreement with the HR-TEM evidence of the very limited contribution of the HA(001) termination to determine the crystalline habit of the HA nanoparticles used[15] and, more importantly, with other theoretical evidence[23] as well as with experimental HRTEM results on other HA nanoparticles[18, 57] of the role of the HA(010)_P-rich and HA(010)_Ca-rich crystal faces to dictate the morphology of HA nano-crystals.

Conclusions

In this paper, quantum-mechanical modeling based on the B3LYP-D* method and experimental IR technique have been adopted to characterize the features of the CO adsorption on four different slab models mimicking the HA most important surfaces, i.e. the stoichiometric HA(001) and HA(010)R (the R stands for "water-reacted") surfaces and the non-stoichiometric HA(010)_Ca-rich and HA(010)_P-rich ones, respectively. The detailed analysis of the computed adsorption enthalpies revealed that electrostatic, polarization, charge transfer and exchange repulsion components of the interaction energy are counter balanced by the London dispersive contribution, resulting in an almost flat enthalpy of adsorption value, peaked at around -20 $kJ \cdot mol^{-1}$, at almost any CO loading higher than 1 CO *per* unit cell. As a consequence, no surface selection, based on energetic criteria, is possible to assess the most relevant surface termination of nanoparticles. Conversely, if the combined use of B3LYP and experimental vibrational features of CO adsorbed at high loadings are considered, elements for the recognition of the surface terminations of HA nanoparticles appeared. Interestingly, the proposed method appear to be able to distinguish not only between different families of surface facets, i.e. {001} and {010}, but, more importantly, to provide information of the relative contribution to the surface terminations of the layers resulting from the stoichiometric, Ca-rich and P-rich of the {010} surfaces, that are usually dictating the morphology of HA nanoparticles.

Acknowledgments

Progetti di Ricerca di Ateneo-Compagnia di San Paolo-2011-Linea 1A, progetto ORTO11RRT5 is acknowledged for funding. Some of the computational results have been obtained using the massive parallel version of the CRYSTAL09 code provided by the Theoretical Chemistry group at Dipartimento di Chimica, Università di Torino. N. Roveri (Dip. Chimica, University of Bologna) and M. Delle Piane are acknowledged for kindly providing the HA sample and for help in using the massive parallel version of CRYSTAL09 code, respectively.

Supporting Information Available

Data on interaction energies, electronic charge transfer, infrared intensities, and the full set of figures are available free of charge via the Internet at http://pubs.acs.org.

Table 1. Energetic features (the apex C means BSSE-corrected value) of the interactions between CO and HA surfaces. ϑ indicates the loading, representing the number of CO per nm^2. ΔE^C is the electronic interaction energy, ΔE^D is the pure dispersive contribution, calculated *a posteriori* with the Grimme's correction; $\Delta E^{CD} = \Delta E^C + \Delta E^D$, $\Delta H(0)$ is the enthalpy at 0 K, $\Delta H(RT)$ is the enthalpy at 293.15 K (i.e. Room Temperature). All data are in kJ mol^{-1}.

Structure	ϑ	$-\Delta E^C$	$-\Delta E^D$	$-\Delta E^{CD}$	$-\Delta H(0)$	$-\Delta H(RT)$
HA(001)						
1CO	1.3	22.7	8.1	30.8	27.3	23.9
2CO	2.7	16.4	11.4	27.8	24.5	21.0
3CO	4.0	14.0	13.4	27.4	24.1	20.6
4CO	5.3	11.9	14.7	26.6	23.0	19.6
HA(010)R						
1CO	1.5	17.0	17.3	34.3	31.0	27.5
2CO	3.0	11.0	12.2	23.2	20.6	16.6
3CO	4.5	6.9	15.8	22.7	19.6	16.0
4CO	6.0	7.3	17.4	24.7	21.3	17.9
HA(010)_Ca-rich						
1CO	1.5	24.7	7.5	32.2	28.7	25.3
2CO	3.0	20.0	12.6	32.6	29.2	25.7
3CO	4.5	17.3	13.9	31.2	27.8	24.4
4CO	6.0	15.1	15.1	30.2	26.7	23.4
HA(010)_P-rich						
1CO	1.5	28.4	13.1	41.5	37.7	34.6
2CO	3.0	19.5	13.0	32.5	28.9	25.7
3CO	4.5	16.7	14.0	30.7	27.0	23.9
4CO	6.0	13.8	14.7	28.5	25.0	23.5

Table 2. Scaled B3LYP CO vibrational stretching frequency (cm^{-1}) for all considered cases. ν(CO gas) = 2143 cm^{-1}.

Structure	**ν(CO)**			
HA(001)				
1CO	2183			
2CO	2188	2155		
3CO	2188	2157	2154	
4CO	2188	2159	2154	2153
HA(010)R				
1CO	2187			
2CO	2186	2160		
3CO	2173	2158	2157	
4CO	2176	2169	2160	2156
HA(010)_Ca-rich				
1CO	2185			
2CO	2185	2173		
3CO	2181	2173	2170	
4CO	2178	2172	2172	2147
HA(010)_P-rich				
1CO	2183			
2CO	2169	2163		
3CO	2169	2160	2157	
4CO	2170	2165	2156	2151

Figure 1. Structures of the B3LYP optimized HA slab structures considered in this work. Ca in grey, oxygen in red, phosphorus in yellow and hydrogen in white. The Ca ions available for CO interaction are labeled by *. Unit cell borders as yellow lines.

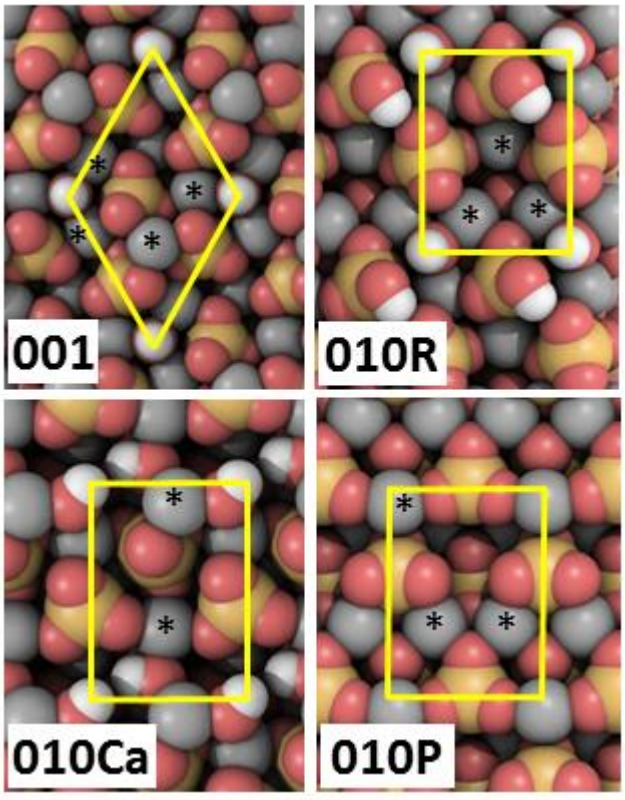

Figure 2. Scaled B3LYP harmonic infrared spectra computed on the basis of data in Table 2 and assuming a bandwidth of 15 cm^{-1} for each component. In each panel are the spectra calculated for 1 (top-left), 2 (top-right), 3(bottom-right) and 4 (bottom-left) CO molecules on the four HA surfaces considered. The color code for the association spectrum-surface is in the top-left panel.

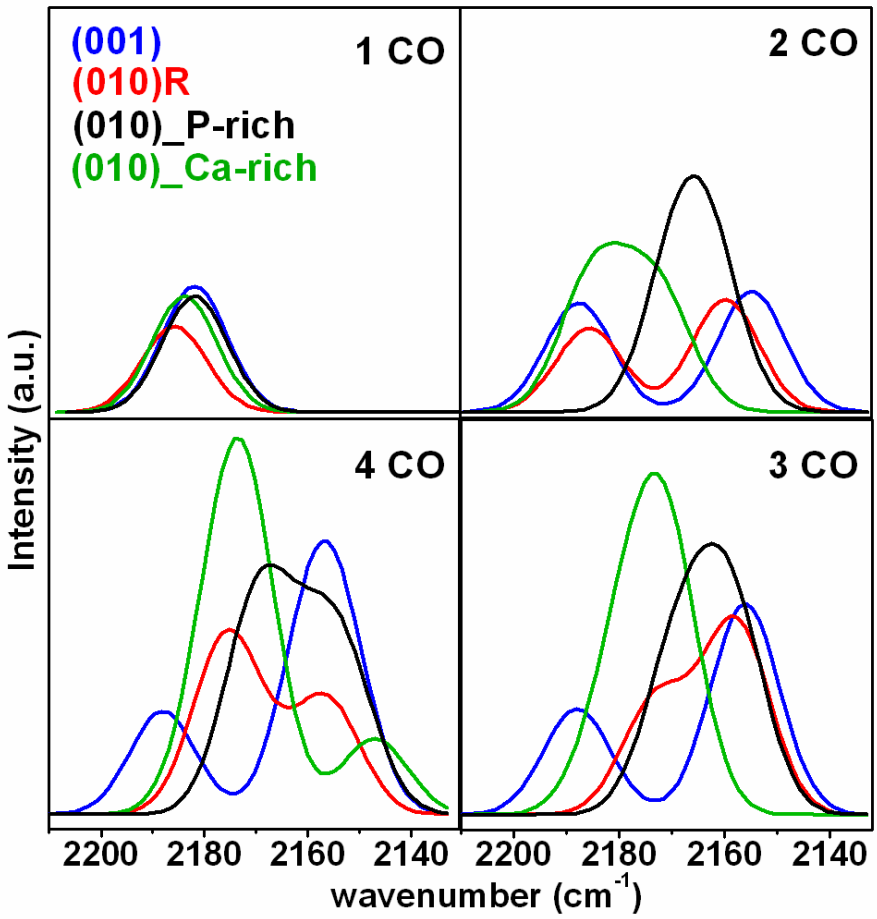

Figure 3. Experimental IR spectra of CO adsorbed at 100 K on HA nanoparticles, from the presence of 10 mbar CO (curve a) to outgassing for 1 min (curve j). The spectra from 25 to 12 mbar CO are not shown because of the even higher intensity of the additional contribution due to CO gas. The lettering is in the sense of decreasing CO coverage, from the presence of 10 mbar CO in equilibrium with the sample to outgassing for 1 min. Insets A and B: zoomed view of the 2150-2125 and 2135-2105 cm^{-1} range, respectively. Note that in inset A the contribution of the roto-vibrational profile of CO gas in equilibrium with the sample is no longer visible from 5 mbar CO (curve c) towards lower coverage. Conversely, in inset B, where the zoom factor along the Y axis is ca. 10 times higher (see the difference in the bar scale), traces of the CO gas profile appeared still contribute to spectrum c.

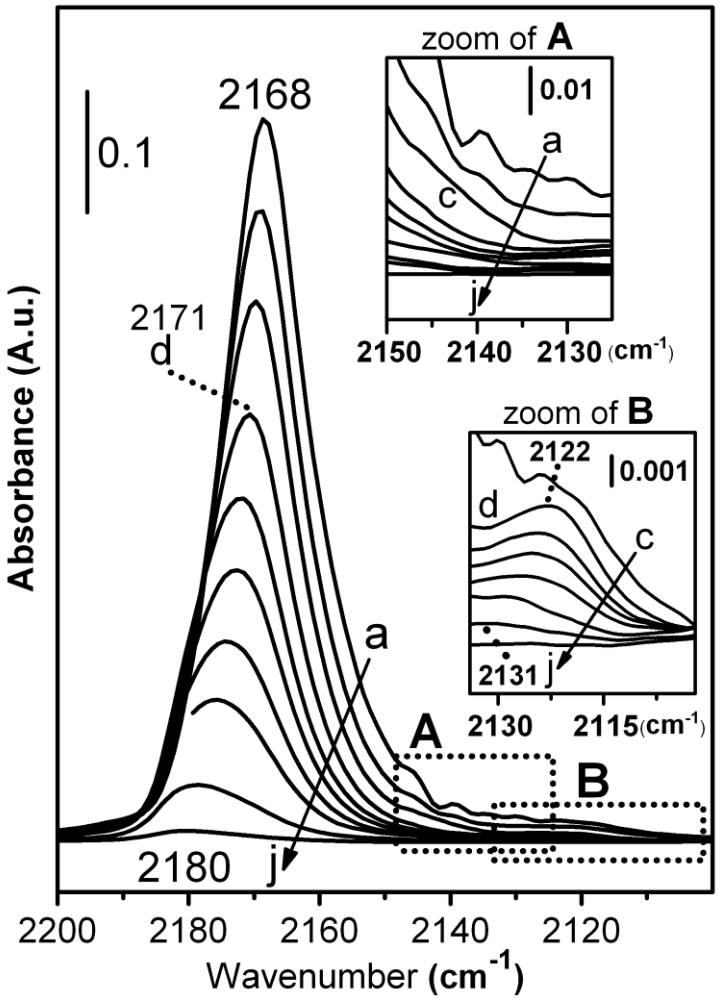

Figure 4. Structures of the 4CO/HA(010)_Ca-rich and the 2CO/HA(010)_P-rich models. Left: balls and sticks side view of the systems. Right: van der Waals top view of the systems. Ca---CO distances, CO vibrational frequencies and the enthalpy values at room temperature are reported. Colors coding as in Figure 1 (carbon in light blue).

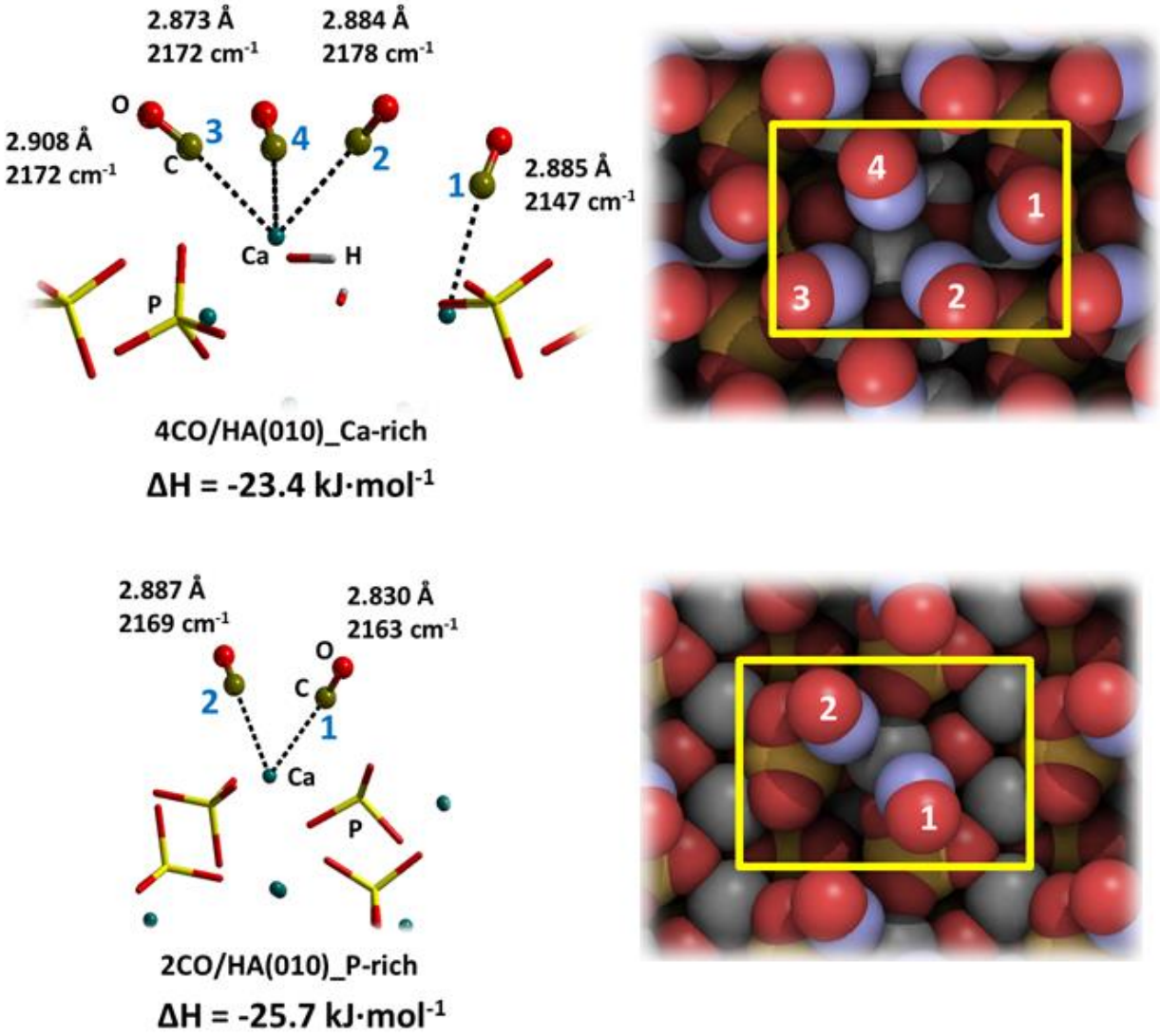

Figure 5. Experimental IR spectrum as black solid line (the same as curve c in Figure 3, *i.e.* the spectrum collected in the presence of 2 mbar CO in equilibrium with the sample at ca. 100 K); red-triangles and black-squares as B3LYP 2CO/HA(010)_P-rich and 4CO/HA(010)_Ca-rich spectra, respectively; black-dot spectrum as sum of B3LYP separated spectra.

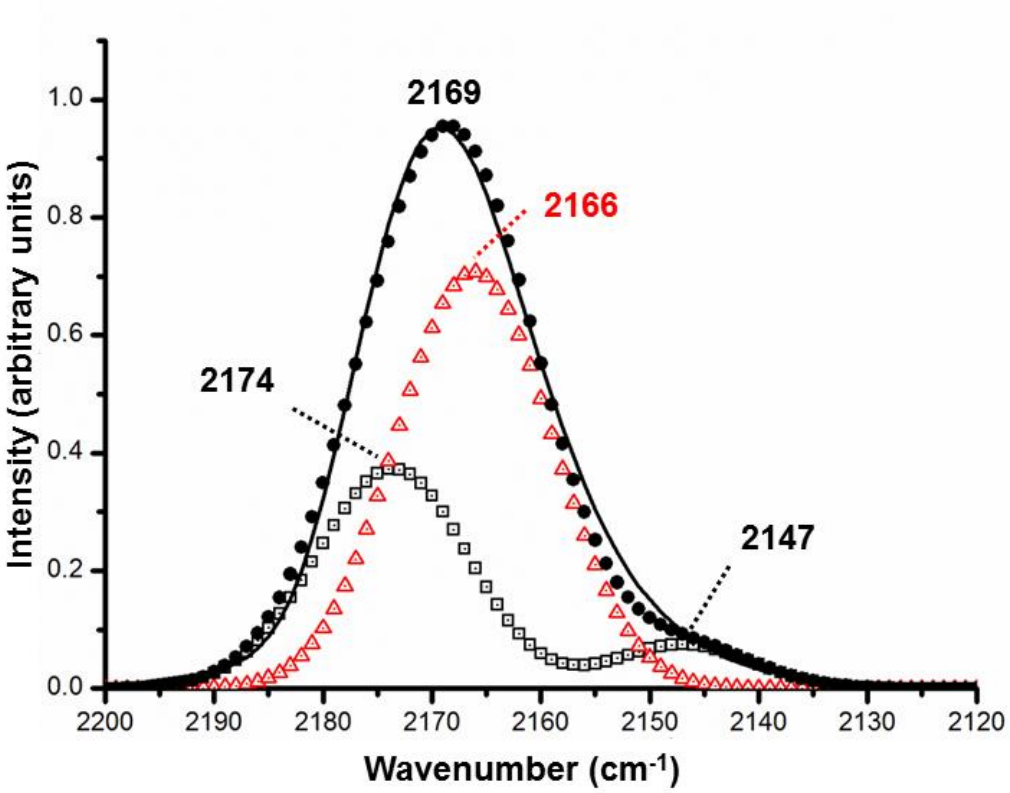

References

1. Hench, L. L., Biomaterials. *Science* **1980,** *208*, 826-831.

2. Dorozhkin, S. V., Nanodimensional and Nanocrystalline Apatites and Other Calcium Orthophosphates in Biomedical Engineering, Biology and Medicine. *Materials* **2009,** *2*, 1975-2045.

3. Roveri, N.; Palazzo, B., Hydroxyapatite Nanocrystals as Bone Tissue Substitute. In *Tissue, Cell and Organ Engineering*, Kumar, C. S. S. R., Ed. Wiley-VCH: Weinheim, 2006; Vol. 9, pp 283-307.

4. Palazzo, B.; Iafisco, M.; Laforgia, M.; Margiotta, N.; Natile, G.; Bianchi, C. L.; Walsh, D.; Mann, S.; Roveri, N., Biomimetic Hydroxyapatite-Drug Nanocrystals as Potential Bone Substitutes with Antitumor Drug Delivery Properties. *Adv. Funct. Mater.* **2007,** *17*, 2180-2188.

5. Gross, K. A.; Berndt, C. C., Thermal processing of hydroxyapatite for coating production. *J. Biomed. Mater. Res.* **1998,** *39*, 580-587.

6. Elliott, J. C., *Structure and Chemistry of the Apatites and Other Calcium Orthophosphates*. Elsevier: Amsterdam, 1994.

7. Yamagishi, K.; Onuma, K.; Suzuki, T.; Okada, F.; Tagami, J.; Otsuki, M.; Senawangse, P., A Synthetic Enamel for Rapid Tooth Repair. *Nature* **2005,** *433*, 819-819.

8. Jaworski, J. W.; Cho, S.; Kim, Y.; Jung, J. H.; Jeon, H. S.; Min, B. K.; Kwon, K.-Y., Hydroxyapatite supported cobalt catalysts for hydrogen generation. *J. Colloid Interface Sci.* **2013,** *394*, 401-8.

9. Zahmaktran, M.; Roman-Leshkov, Y.; Zhang, Y., Rhodium(0) Nanoparticles Supported on Nanocrystalline Hydroxyapatite: Highly Effective Catalytic System for the Solvent-Free Hydrogenation of Aromatics at Room Temperature. *Langmuir* **2012,** *28*, 60-64.

10. Tsuchida, T.; Kubo, J.; Yoshioka, T.; Sakuma, S.; Takeguchi, T.; Ueda, W., Reaction of ethanol over hydroxyapatite affected by Ca/P ratio of catalyst. *J. Catal.* **2008,** *259*, 183-189.

11. Tsuchida, T.; Yoshioka, T.; Sakuma, S.; Takeguchi, T.; Ueda, W., Synthesis of biogasoline from ethanol over hydroxyapatite catalyst. *Ind. Eng. Chem. Res.* **2008,** *47*, 1443-1452.

12. Liptáková, B.; Hronec, M.; Cvengrošová, Z., Direct synthesis of phenol from benzene over hydroxyapatite catalysts. *Catal. Today* **2000,** *61*, 143–148.

13. Kandori, K.; Fudo, A.; Ishikawa, T., Study on the particle texture dependence of protein adsorption by using synthetic micrometer-sized calcium hydroxyapatite particles. *Colloids Surf., B* **2002,** *24*, 145-153.

14. Reynolds, E. C.; Wong, A., Effect of adsorbed protein on hydroxyapatite zeta potential and Streptococcus mutans adherence. *Infect. Immun.* **1983,** *39*, 1285-90.

15. Sakhno, Y.; Bertinetti, L.; Iafisco, M.; Tampieri, A.; Roveri, N.; Martra, G., Surface hydration and cationic sites of nanohydroxyapatites with amorphous or crystalline surfaces: a comparative study. *J. Phys. Chem. C* **2010,** *114*, 16640-16648.

16. Bertinetti, L.; Tampieri, A.; Landi, E.; Ducati, C.; Midgley, P. A.; Coluccia, S.; Martra, G., Surface structure, hydration, and cationic sites of nanohydroxyapatite: UHR-TEM, IR, and microgravimetric studies. *J. Phys. Chem. C* **2007,** *111*, 4027-4035.

17. Sato, K.; Kogure, T.; Iwai, H.; Tanaka, J., Atomic-Scale {1010} Interfacial Structure in Hydroxyapatite Determined by High-Resolution Transmission Electron Microscopy. *J. Am. Ceram. Soc.* **2002,** *85*, 3054-3058.

18. Ospina, C. A.; Terra, J.; Ramirez, A. J.; Farina, M.; Ellis, D. E.; Rossi, A. M., Experimental evidence and structural modeling of nonstoichiometric (010) surfaces coexisting in hydroxyapatite nano-crystals. *Colloids Surf., B* **2012,** *89*, 15-22.

19. Rimola, A.; Sakhno, Y.; Bertinetti, L.; Lelli, M.; Martra, G.; Ugliengo, P., Toward a Surface Science Model for Biology: Glycine Adsorption on Nanohydroxyapatite with Well-Defined Surfaces. *J. Phys. Chem. Lett.* **2011,** *2*, 1390-1394.

20. Jimenez-Izal, E.; Chiatti, F.; Corno, M.; Rimola, A.; Ugliengo, P., Glycine Adsorption at Non-Stoichiometric (010) Hydroxyapatite Surfaces: a B3LYP study. *J. Phys. Chem. C* **2012,** *116*, 14561-14567.

21. Zecchina, A.; Otero Arean, C., Diatomic Molecular Probes for Mid-IR Studies of Zeolites. *Chem. Soc. Rev.* **1996,** *25*, 187-197.

22. Bolis, V.; Busco, C.; Martra, G.; Bertinetti, L.; Sakhno, Y.; Ugliengo, P.; Chiatti, F.; Corno, M.; Roveri, N., Coordination Chemistry of Ca Sites at the Surface of Nanosized Hydroxyapatite: Interaction with H_2O and CO. *Phil. Trans. R. Soc. A* **2012,** *370*, 1313-1336.

23. Astala, R.; Stott, M. J., First-principles study oh hydroxyapatite surfaces and water adsorption. *Phys. Rev. B* **2008,** *78*, 075427-075437.

24. Marchese, L.; Bordiga, S.; Coluccia, S.; Martra, G.; Zecchina, A., Structure of the Surface Sites of δ-Al_2O_3 as Determined by High-Resolution Transmission Electron-Microscopy, Computer Modeling and Infrared-Spectroscopy of Adsorbed CO. *J. Chem. Soc., Faraday Trans.* **1993,** *89*, 3483-3489.

25. Dovesi, R.; Orlando, R.; Civalleri, B.; Roetti, C.; Saunders, V. R.; Zicovich-Wilson, C. M., CRYSTAL: a computational tool for the ab initio study of the electronic properties of crystals. *Z. Kristallogr.* **2005,** *220*, 571-573.

26. Dovesi, R.; Saunders, V. R.; Roetti, C.; Orlando, R.; Zicovich-Wilson, C. M.; Pascale, F.; Civalleri, B.; Doll, K.; Harrison, N. M.; Bush, I. J.; D'Arco, P.; Llunell, M. University of Turin: CRYSTAL2009 User's Manual. Turin, 2009.

27. Ugliengo, P.; Viterbo, D.; Chiari, G., MOLDRAW: Molecular Graphics on a Personal Computer. *Z. Kristallogr.* **1993,** *207*, 9-23.

28. Tarini, M.; Cignoni, P.; Montani, C., Ambient Occlusion and Edge Cueing for Enhancing Real Time Molecular Visualization. *IEEE Trans. Vis. Comput. Graph.* **2006,** *12*, 1237-1244.

29. Catti, M.; Pavese, A.; Saunders, V. R., Elastic constants and electronic structure of fluorite (CaF_2): an ab initio Hartree-Fock study. *J. Phys.: Condens. Matter* **1991,** *3*, 4151-4164.

30. Schafer, A.; Horn, H.; Ahlrichs, R., Fully optimized contracted Gaussian basis set for atom Li to Kr. *J. Chem. Phys.* **1992,** *97*, 2571-2577.

31. Corno, M.; Chiatti, F.; Pedone, A.; Ugliengo, P., In Silico Study of Hydroxyapatite and Bioglass®: How Computational Science Sheds Light on Biomaterials. In *Biomaterials - Physics and Chemistry*, Pignatello, R., Ed. InTech: 2011; pp 275-298.

32. Corno, M.; Busco, C.; Bolis, V.; Tosoni, S.; Ugliengo, P., Water Adsorption on the Stoichiometric (001) and (010) Surfaces of Hydroxyapatite: A Periodic B3LYP Study. *Langmuir* **2009,** *25*, 2188-2198.

33. Corno, M.; Orlando, R.; Civalleri, B.; Ugliengo, P., Periodic B3LYP Study of Hydroxyapatite (001) Surface Modelled by Thin Layer Slab. *Eur. J. Mineral.* **2007,** *19*, 757-767.

34. Rimola, A.; Sodupe, M.; Tosoni, S.; Civalleri, B.; Ugliengo, P., Interaction of Glycine with Isolated Hydroxyl Groups at the Silica Surface: First Principles B3LYP Periodic Simulation. *Langmuir* **2006,** *22*, 6593-6604.

35. Civalleri, B.; Zicovich-Wilson, C. M.; Valenzano, L.; Ugliengo, P., B3LYP augmented with an empirical dispersion term (B3LYP-D*) as applied to molecular crystals. *CrystEngComm* **2008,** *10*, 405-410.

36. Grimme, S., Semiempirical GGA-Type Density Functional Constructed with a Long-Range Dispersion Correction. *J. Comput. Chem.* **2006,** *27*, 1787-1799.

37. Pascale, F.; Zicovich-Wilson, C. M.; Gejo, F. L.; Civalleri, B.; Orlando, R.; Dovesi, R., The calculation of the vibrational frequencies of crystalline compounds and its implementation in the CRYSTAL code. *J. Comput. Chem.* **2004,** *25*, 888-897.

38. Tosoni, S.; Pascale, F.; Ugliengo, P.; Orlando, R.; Saunders, V. R.; Dovesi, R., Quantum mechanical calculation of the OH vibrational frequency in crystalline solids. *Mol. Phys.* **2005,** *103*, 2549-2558.

39. Rimola, A.; Civalleri, B.; Ugliengo, P., Neutral vs Zwitterionic Glycine Forms at the Water/Silica Interface: Structure, Energies, and Vibrational Features from B3LYP Periodic Simulations. *Langmuir* **2008,** *24*, 14027-14034.

40. Noel, Y.; Zicovich-Wilson, C. M.; Civalleri, B.; D'Arco, P.; Dovesi, R., Polarization Properties of ZnO and BeO: an Ab Initio Study through the Berry Phase and Wannier Functions Approaches. *Phys. Rev. B.* **2001,** *65*, 014111-014120.

41. Ulian, G.; Valdré, G.; Corno, M.; Ugliengo, P., The Vibrational Features of Hydroxylapatite and Type A Carbonated Apatite: A First Principle Contribution. *Am. Mineral.* **2013,** *98*, 752-759.

42. Ulian, G.; Valdre, G.; Corno, M.; Ugliengo, P., Periodic ab initio Bulk Investigation of Hydroxylapatite and Type A Carbonated Apatite with both Pseudopotential and All-electron Basis Sets for Calcium Atoms. *Am. Mineral.* **2013,** *98*, 410-416.

43. Corno, M.; Rimola, A.; Bolis, V.; Ugliengo, P., Hydroxyapatite as a Key Biomaterial: Quantum-Mechanical Simulation of its Surfaces in Interaction with Biomolecules. *Phys. Chem. Chem. Phys.* **2010,** *12*, 6309-6329.

44. Chiatti, F.; Corno, M.; Ugliengo, P., Stability of the Dipolar (001) Surface of Hydroxyapatite. *J. Phys. Chem. C* **2012,** *116*, 6108-6114.

45. Canepa, P.; Chiatti, F.; Corno, M.; Sakhno, Y.; Martra, G.; Ugliengo, P., Affinity of Hydroxyapatite (001) and (010) Surfaces to Formic and Alendronic Acids: a Quantum-Mechanical and Infrared Study. *Phys. Chem. Chem. Phys.* **2011,** *13*, 1099-1111.

46. Rimola, A.; Aschi, M.; Orlando, R.; Ugliengo, P., Does Adsorption at Hydroxyapatite Surfaces Induce Peptide Folding? Insights from Large-Scale B3LYP Calculations. *J. Am. Chem. Soc.* **2012,** *134*, 10899-10910.

47. Lukes, V.; Laurinc, V.; Ilcin, M.; Biskupic, S., Ab initio study of the Li-CO van der Waals complex. *Collect. Czech. Chem. Commun.* **2003,** *68*, 35-46.

48. Vandiver, J.; Dean, D.; Patel, N.; Botelho, C.; Best, S.; Santos, J. D.; Lopes, M. A.; Bonfield, W.; Ortiz, C., Silicon addition to hydroxyapatite increases nanoscale electrostatic, van der Waals, and adhesive interactions. *J. Biomed. Mater. Res., Part A* **2006,** *78A*, 352-363.

49. Zecchina, A.; Otero Arean, C.; Turnes Palomino, G.; Geobaldo, F.; Lamberti, C.; Spoto, G.; Bordiga, S., The Vibrational Spectroscopy of H_2, N_2, CO and NO Adsorbed on the Titanosilicate Molecular Sieve ETS-10. *Phys. Chem. Chem. Phys.* **1999,** *1*, 1649-1657.

50. Martra, G.; Ocule, R.; Marchese, L.; Centi, G.; Coluccia, S., Alkali and Alkaline-Earth Exchanged Faujasites: Strength of Lewis Base and Acid Centres and Cation Site Occupancy in Na- and BaY and Na- and BaX Zeolites. *Catal. Today* **2002,** *73*, 83-93.

51. Pelmenschikov, A.; Morosi, G.; Gamba, A.; Coluccia, S.; Martra, G.; Pettersson, L. G. M., Can the Three-Coordinated Mg Site of MgO Accomodate More than One CO Molecule? *J. Phys. Chem. B* **2000,** *104*, 11497-11500.

52. Costa, D.; Martra, G.; Che, M.; Manceron, L.; Kermarec, M., IR and Theoretical Studies of Monocarbonyl Ni Complexes Formed by Adsorption of CO at Low Pressure on Silica-Supported NiII Ions. *J. Am. Chem. Soc.* **2002,** *124*, 7210-7217.

53. Martra, G.; Coluccia, S.; Che, M.; Manceron, L.; Kermarec, M.; Costa, D., Ni and CO Used as Probes of the Amorphous Silica Surface: IR and Theoretical Studies of Dicarbonyl NiII Complexes. *J. Phys. Chem. B* **2003,** *107*, 6096-6104.

54. Zecchina, A.; Scarano, D.; Garrone, E., Dynamic and static interactions in CO overlayers on sintered NaCl films. *Surf. Sci.* **1985,** *160*, 492-508.

55. Marchese, L.; Coluccia, S.; Martra, G.; Zecchina, A., Dynamic and static interactions in CO layers adsorbed on MgO smoke (100) facelets: a FTIR and HRTEM study. *Surf. Sci.* **1992,** *269–270*, 135-140.

56. Deiana, C.; Minella, M.; Tabacchi, G.; Maurino, V.; Fois, E.; Martra, G., Shape-controlled TiO_2 nanoparticles and TiO_2 P25 interacting with CO and H_2O_2 molecular probes: a synergic approach for surface structure recognition and physico-chemical understanding. *Phys. Chem. Chem. Phys.* **2013,** *15*, 307-315.

57. Sato, K.; Kogure, T.; Kumagai, Y.; Tanaka, J., Crystal Orientation of Hydroxyapatite Induced by Ordered Carboxyl Groups. *J. Colloid. Interf. Sci.* **2001,** *240*, 133-138.

Table of Contents Graphic